ChemComm

ROYAL SOCIETY OF CHEMISTRY

COMMUNICATION

View Article Online
View Journal | View Issue

Cite this: *Chem. Commun.*, 2025, **61**, 10126

Received 12th February 2025,
Accepted 27th May 2025

DOI: 10.1039/d5cc00792e

rsc.li/chemcomm

Self-assembly of ruthenium-doped oxygen-deficient tungsten oxide as an efficient electrocatalyst for the hydrogen evolution reaction in acidic environments†

Elhussein Desoki Helal,‡[ab] Wenhai Xu,‡[a] Yizhe Li,[a] Liyao Gao,[a] Hao Sun,[a] Qingzhen Xu,[a] Imran Ali Chandio,[a] Safdar Abbas,[a] Abdul Hameed Pato[a] and Wen Liu *[a]

Urchin-like Ru-doped $W_{18}O_{49}$ nanospheres assembled from nanorods are synthesized *via* a straightforward hydrothermal process. The resultant electrocatalyst, with very low Ru content of 3.2 wt%, exhibits outstanding performance for the acidic HER. The remarkable performance can be attributed to the Ru dopants, and the distinctive urchin-like hierarchical nanostructure.

Platinum is deemed as the best material for the hydrogen evolution reaction (HER) in proton exchange membrane (PEM) water electrolyzers because of its optimal binding energy with hydrogen intermediates (H*).[1] However, the expensive cost, limited availability, and substantial loading requirements of Pt hinder the large-scale application and development of PEM electrolyzers.[2,3] To overcome this challenge, extensive research has focused on the design and synthesis of inexpensive, and efficient alternatives to Pt.[4–6] Tungsten oxide (WO_3) is a typical n-type semiconductor compound that features great stability in acid even at high potential.[7] However, it suffers from the low kinetics of electron transfer, handicapping the interaction of electrons with H^+ ions during the HER. With the increase of oxygen vacancies, the compound gradually transforms from a semiconductor to a conductor because of the up-shift of the Fermi level that can even cross the conduction band, suggesting an enhanced electron transfer.[8] Besides, the oxygen vacancies strategy is a facile method to strengthen the adsorption of hydrogen, which can compensate the weak hydrogen adsorption of stoichiometric WO_3 and improve catalytic activity.[9,10] One of the non-stoichiometric tungsten oxides due to abundant oxygen vacancies is $W_{18}O_{49}$, which has varied oxidation state of W, exhibiting unique properties such as high electrical conductivity and the existence of coordinatively unsaturated cationic sites. These sites not only facilitate electron transport within the oxide network, but also enhance the synergistic effect during the catalytic process.[11] However, its intrinsic activity for the HER is relatively low, necessitating further modifications to enhance its catalytic performance. One effective strategy to improve the electrocatalytic properties of tungsten oxide is doping with other metals, which can tailor the electronic structure and create more active sites. Recent studies have demonstrated that doping tungsten oxide with transitional metals can significantly enhance its catalytic activity. Inspired by these properties, we hypothesize that doping $W_{18}O_{49}$ with ruthenium (Ru) could be a promising electrocatalyst for the HER. As Ru is relatively more abundant and less expensive than platinum, it offers a viable alternative while still providing excellent catalytic properties.

Herein, urchin-like Ru–$W_{18}O_{49}$ nanospheres assembled from nanorods were synthesized using a facile one-pot hydrothermal method. This method involved tungsten(VI) chloride (WCl_6), ruthenium(III) chloride hexahydrate ($RuCl_3·6H_2O$), and absolute ethanol as metal precursors and solvent, respectively, followed by heat treatment at 180 °C for 24 h. The resulting products are denoted as Ru–$W_{18}O_{49}$-(x%), where x% refers to the feeding molar ratio of $RuCl_3·6H_2O$. The powder X-ray diffraction (XRD) patterns (Fig. 1A) display two distinctive diffraction peaks centered at 23.5° and 48.1°, corresponding to the (010), and (020) crystalline planes, respectively, of the monoclinic $W_{18}O_{49}$ phase (JCPDS 05-0392). The incorporation of Ru does not alter the monoclinic structure, nor does it introduce any additional diffraction peaks related to Ru metal crystallinity or impurities. Notably, the characteristic peak at $2\theta = 23.5^\circ$ is slightly shifted to lower angles upon Ru introduction compared to pristine $W_{18}O_{49}$ (Fig. 1B), indicating successful doping of Ru into the crystal structure of $W_{18}O_{49}$. This shift is attributed to lattice expansion due to the relatively larger ionic radius of Ru compared to that of W ions. The prominent diffraction peak at 23.5° in the XRD patterns of all samples, which corresponds to the (010) crystal

---

[a] *State Key Laboratory of Chemical Resource Engineering, College of Chemistry, Beijing University of Chemical Technology, Beijing, 100092, China. E-mail: wenliu@mail.buct.edu.cn*

[b] *Chemistry Department, Faculty of Science, Benha University, Benha, 13518, Egypt*

† Electronic supplementary information (ESI) available. See DOI: https://doi.org/10.1039/d5cc00792e

‡ These authors contributed equally to this work.

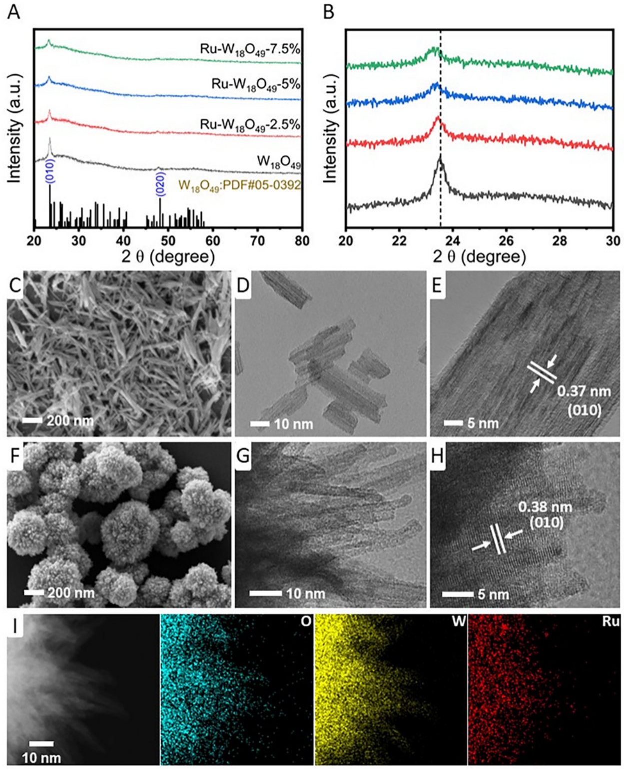

Fig. 1 Morphological and structural characterization of the catalysts. (A) XRD patterns of pristine $W_{18}O_{49}$ and Ru–$W_{18}O_{49}$ samples and (B) extended XRD patterns of A. (C) SEM image, (D) TEM image, (E) HR-TEM image of $W_{18}O_{49}$. (F) SEM image, (G) TEM image, (H) HR-TEM image, and (I) elemental mapping at a 10 nm scale by HAADF-STEM of Ru–$W_{18}O_{49}$-5%.

plane, strongly indicates that the crystal growth predominantly occurs along the [010] direction.[12] Scanning electron microscopy (SEM) images reveal that the pristine $W_{18}O_{49}$ exhibits radial nanorods (Fig. 1C). Adding $RuCl_3{\cdot}6H_2O$ during the synthesis process drives these nanorods to assemble urchin-like nanospheres, as shown in SEM and transmission electron microscope (TEM) images (Fig. 1F, G and Fig. S2, ESI†). It is worth noting that no distinct Ru crystallinity is observed (Fig. 1G), further validating the results of XRD. High-resolution transmission electron microscope (HR-TEM) images (Fig. 1E and H) show an increase in the lattice spacing upon Ru addition, indicating to lattice expansion and further confirming Ru doping. The selected area electron diffraction (SAED) pattern of Ru–$W_{18}O_{49}$-5% is shown in Fig. S2 (ESI†). Elemental analysis using energy-dispersive X-ray spectroscopy (EDX) based on SEM confirms the presence of Ru, W, and O in the sample (Fig. S2, ESI†). Additionally, high-angle annular dark field-scanning transmission electron microscopy (HAADF-STEM) based elemental mapping images at a scale of 10 nm (Fig. 1I) show that Ru, W, and O elements are evenly dispersed throughout the sample. Inductively coupled plasma optical emission spectrometry (ICP-OES) was conducted and the test results (Table S1, ESI†) indicate that Ru–$W_{18}O_{49}$-5% contains 3.2 wt% of Ru and 78.2 wt% of W.

X-ray photoelectron spectroscopy (XPS) was employed to reveal the as-prepared catalysts' electronic structure. The high-resolution XPS spectrum of W 4f for $W_{18}O_{49}$ (Fig. 2A) was deconvoluted into four peaks, corresponding to two different oxidation states of W: W^{5+} (34.75 and 36.77 eV), and W^{6+} (35.73 and 37.89 eV).[13] The simultaneous existence of both W^{6+} and W^{5+} species is ascribed to the corner-sharing and edge-sharing W sites in the $[WO_6]$ octahedron.[14] Notably, the W 4f peaks shifted to lower binding energies due to the introduction of Ru ions, revealing that W^{6+} species were reduced to lower oxidation state species, W^{5+}, as evidenced by W L_3-edge XANES spectra (Fig. S3, ESI†).[15] Moreover, the proportions of both W^{5+} and W^{6+} in $W_{18}O_{49}$ and Ru–$W_{18}O_{49}$-5% were determined from the peak areas and it was found that the W^{5+} percentage in Ru–$W_{18}O_{49}$-5% substantially increased compare to that in $W_{18}O_{49}$ (Table S2, ESI†), further affirming the decline in the catalyst's average valence. The O 1s high resolution XPS spectrum (Fig. 2B) was deconvoluted into three peaks, representing the lattice oxygen species (O_L), oxygen vacancy species (O_V), and surface chemisorbed oxygen species (O_C). In the case of $W_{18}O_{49}$, the dominant peak is for O_L, centered at around 530.42 eV, while the peak located at around 531.57 eV is ascribed to O_V indicative of oxygen defects in the sample, and the peak at around 533.03 eV is attributed to O_C due to adsorbed OH groups and H_2O molecules on the surface.[16–18] After Ru incorporation, the O 1s peak shifted to lower binding energy and the proportion of oxygen species showed no significant difference compared to those of $W_{18}O_{49}$. Both W 4f and O 1s XPS peaks shifted to lower binding energies after Ru doping, providing strong evidence for electron transfer from Ru to $W_{18}O_{49}$ and modulating the electronic structure of $W_{18}O_{49}$ through charge compensation. The high resolution XPS spectrum of Ru 3p (Fig. 2C) shows two sharp peaks of Ru $3p_{3/2}$ and Ru $3p_{1/2}$ core levels at around 464 and 486 eV, respectively, indicating the presence of a high-valence state of Ru^{4+} doped in

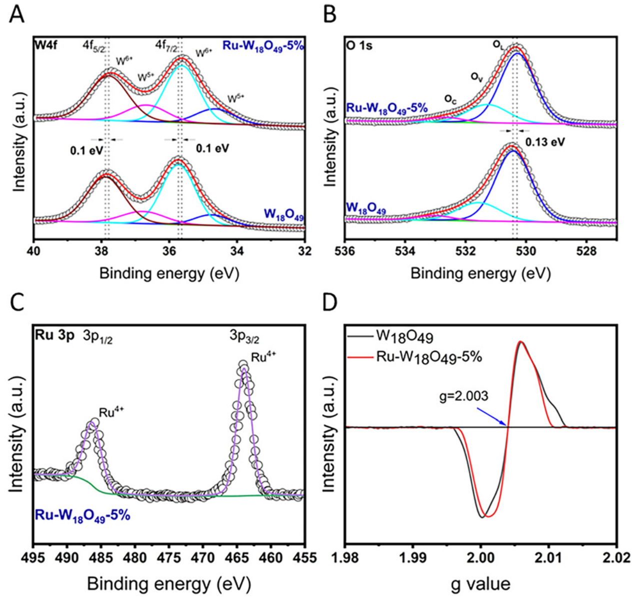

Fig. 2 XPS data of $W_{18}O_{49}$ and Ru–$W_{18}O_{49}$-5%. (A) The high-resolution deconvoluted W 4f, (B) the high-resolution deconvoluted O 1s and (C) the high-resolution deconvoluted Ru 3p XPS spectra, and (D) EPR results.

the $W_{18}O_{49}$ matrix.[15] The variations of the XPS peaks of Ru–$W_{18}O_{49}$-2.5% and Ru–$W_{18}O_{49}$-7.5% were similar to Ru–$W_{18}O_{49}$-5%, except for the existence of Ru metal peaks for Ru–$W_{18}O_{49}$-7.5% due to the excessive addition of Ru (Fig. S4, ESI†). Electron paramagnetic resonance (EPR) tests, as shown in Fig. 2D, show that both $W_{18}O_{49}$ and Ru–$W_{18}O_{49}$ have an obvious symmetric peak at $g \approx 2.003$, which is a typical oxygen vacancy peak,[19] further proving the presence of abundant oxygen vacancies in these structures. However, the peak intensity in Ru–$W_{18}O_{49}$ is roughly similar to that in $W_{18}O_{49}$ suggesting that the percent of oxygen vacancies did not change significantly.

The electrocatalytic performance of the synthesized samples, $W_{18}O_{49}$, Ru–$W_{18}O_{49}$-2.5%, Ru–$W_{18}O_{49}$-5%, and Ru–$W_{18}O_{49}$-7.5% along with commercial benchmarks (20 wt%-Pt/C and 5 wt%-Ru/C) was evaluated for the HER under acidic conditions (0.5 M H_2SO_4) using a three-electrode configuration. Fig. 3A illustrates the *iR*-corrected linear sweep voltammetry (LSV) curves for all catalysts. Pure $W_{18}O_{49}$ displayed a very low HER current, even at a high overpotential, demonstrating poor catalytic performance. In contrast, Ru–$W_{18}O_{49}$-5% showed an overpotential of 36 mV to achieve the benchmark current density of 10 mA cm^{-2}, close to the 31 mV required by commercial 20 wt%-Pt/C, and significantly lower than the overpotentials for Ru–$W_{18}O_{49}$-2.5% (108 mV), and Ru–$W_{18}O_{49}$-7.5% (40 mV) (Fig. S5, ESI†). Ru–$W_{18}O_{49}$-5% had a Tafel slope of 33.8 mV dec^{-1}, close to the 29 mV dec^{-1} for commercial 20 wt%-Pt/C, indicating fast HER kinetics (Fig. 3B). In comparison, $W_{18}O_{49}$, Ru–$W_{18}O_{49}$-2.5%, and Ru–$W_{18}O_{49}$-7.5% had Tafel slopes of 320.6 mV dec^{-1}, 81.2 mV dec^{-1}, and 37.8 mV dec^{-1}, respectively. The lower Tafel slope of Ru–$W_{18}O_{49}$-5% suggests faster increase in HER rate with rising overpotentials, making it favorable for applications. Importantly, the Tafel slope value of Ru–$W_{18}O_{49}$-5% falls in the range of (30–40) mV dec^{-1} indicating that the HER follows the Volmer–Tafel pathway (Fig. S6, ESI†).[20] To further probe the intrinsic activity, the electrochemical specific surface area (ECSA), specific activity, mass activity and turnover frequency (TOF) were measured. The catalyst's double-layer capacitance (C_{dl}) is directly proportional to its ECSA. As shown in Fig. S7 (ESI†), CV curves in the non-faradaic potential window with raising scan speeds were used to estimate C_{dl} values. 1.23 mF cm^{-2} was achieved for Ru–$W_{18}O_{49}$-5%, higher than the values for Ru–$W_{18}O_{49}$-7.5%, 1.17 mF cm^{-2}, Ru–$W_{18}O_{49}$-2.5%, 1.01 mF cm^{-2}, and $W_{18}O_{49}$, 0.6 mF cm^{-2}, indicating more active sites for the HER in Ru–$W_{18}O_{49}$-5% (Fig. S5, ESI†). Moreover, the LSV curves normalized to the electrochemically active surface area, which is defined as the specific activity, were calculated and the Ru–$W_{18}O_{49}$-5% still demonstrated superior HER activity compared to the other samples (Fig. S8, ESI†). Additionally, Ru–$W_{18}O_{49}$-5% showed the highest mass activity of 3620 $A g_{Ru}^{-1}$ at 0.1 V *vs.* RHE, which is 1.48, 8.82, and 16.3 fold higher than that of Ru–$W_{18}O_{49}$-7.5%, Ru–$W_{18}O_{49}$-2.5%, and Ru/C, respectively (Fig. 3C and Fig. S8, ESI†). Furthermore, the turnover frequency (TOF), a critical parameter for intrinsic activity, was calculated based on the Ru content in the catalyst. Ru–$W_{18}O_{49}$-5% had a TOF of 2 s^{-1} at an overpotential of 100 mV, higher than that of Ru–$W_{18}O_{49}$-2.5% (0.22 s^{-1}) and Ru–$W_{18}O_{49}$-7.5% (1.3 s^{-1}) (Fig. S8, ESI†). The stability of the best-performing catalyst Ru–$W_{18}O_{49}$-5% was assessed *via* the chronopotentiometry test (CP) at a 100 mA cm^{-2} current density. The catalyst showed only an 8% decay after 60 hours (Fig. 3D), indicating excellent stability for continuous HER. The structure and morphology of the catalyst after the stability test are clarified in the ESI† (Fig. S9–S11). To investigate the hydrophilicity and bubble detachment behavior of the catalysts, contact angle (CA) measurements were performed using a microinjector to inject approximately 3 μL of gas onto the electrode surface in an H_2SO_4 solution (Fig. 4A). The CA values for Ru–$W_{18}O_{49}$-5%, pristine $W_{18}O_{49}$, and commercial 5 wt% Ru/C were determined to be 32.0°, 40.7°, and 39.0°, respectively (Fig. 4B). The contact angle for Ru–$W_{18}O_{49}$-5% was 7° less than that for commercial 5 wt% Ru/C, indicating higher hydrophilicity and easier bubble detaching which in turn contribute to its high HER rate.

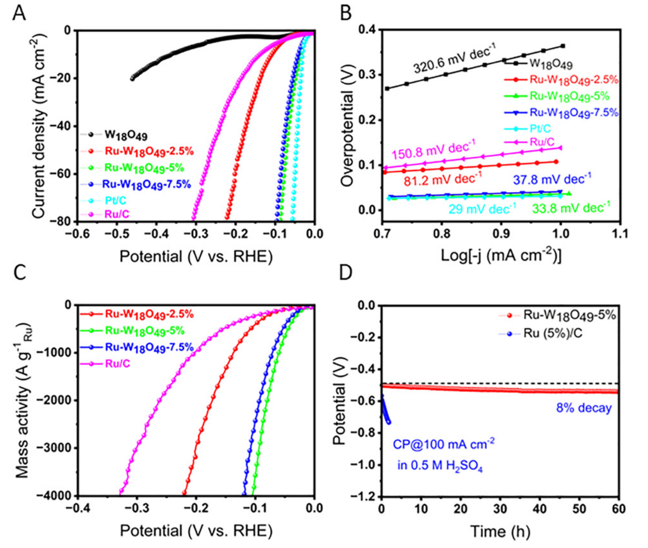

Fig. 3 Catalytic HER performances of the as-prepared samples and commercial samples of Pt/C, and Ru/C in 0.5 M aqueous H_2SO_4 solution: (A) polarization curves, (B) Tafel plots, (C) mass activity, and (D) chronopotentiometry (CP) test of Ru–$W_{18}O_{49}$-5% at 100 mA cm^{-2} for 60 h.

Density functional theory (DFT) calculations were performed to further understand the exceptional HER performance of Ru–$W_{18}O_{49}$-5%. Based on experimental data, a model for Ru-doped $W_{18}O_{49}$-5% was constructed, as shown in Fig. 4C. The HER performance was assessed by comparing hydrogen (H) adsorption energies on both $W_{18}O_{49}$ and Ru-doped $W_{18}O_{49}$ electrocatalysts. The adsorption energy values were found to be 0.0036 eV for Ru–$W_{18}O_{49}$-5%, −0.37 eV for $W_{18}O_{49}$, and 0.224 eV for Ru–$W_{18}O_{49}$-7.5% (Fig. 4D). The hydrogen adsorption energy, as proposed by Nørskov *et al.*, is widely recognized as a key descriptor for predicting catalyst performance in the HER, with an optimal binding strength being crucial for efficient catalytic activity.[21] These results suggest that Ru–$W_{18}O_{49}$-5% exhibits the most favorable H adsorption and desorption characteristics, which are crucial for enhancing HER efficiency. The smallest hydrogen adsorption energy among four possible active sites in Ru–$W_{18}O_{49}$-5% indicates that the Ru dopant site is the active site (Fig. S12, ESI†). Further analysis of the density

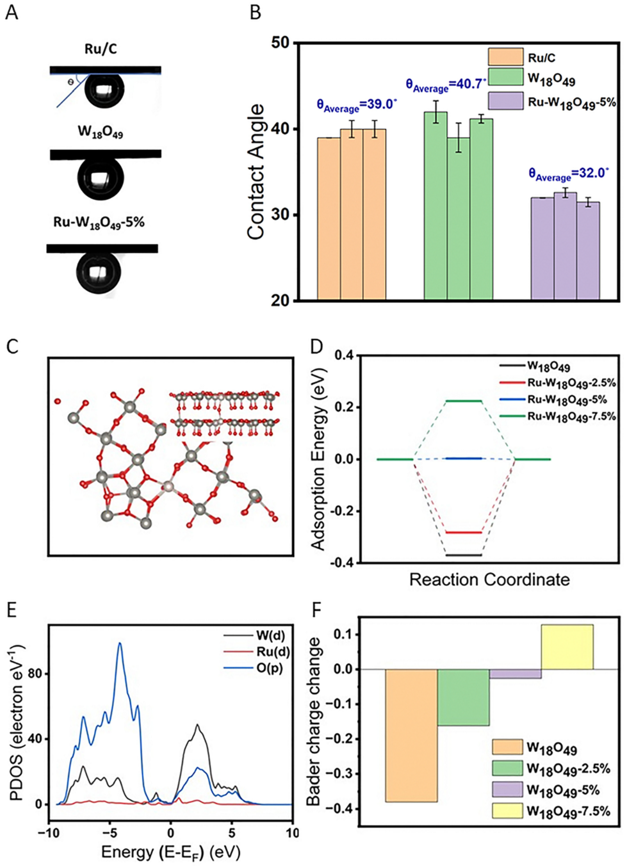

Fig. 4 Mechanism analysis. (A) Bubble contact on the surface of different catalysts; (B) average values of bubble contact angles from three measurements for different catalysts, (C) the top view model and emmetropia model (inset) of Ru–$W_{18}O_{49}$-5% (the red balls represent oxygen atoms, grey balls represent tungsten atoms and silver balls represent ruthenium atoms), (D) comparison of the hydrogen adsorption on different surface models, (E) projected density of states (PDOS) of Ru, W, and O atoms at Ru–$W_{18}O_{49}$-5%, and (F) Bader charge change of $W_{18}O_{49}$ and Ru-doped $W_{18}O_{49}$ before and after adsorption.

of states (DOS) revealed significant orbital overlap among Ru, W, and O in Ru–$W_{18}O_{49}$-5% (Fig. 4E), suggesting a strong interaction between Ru dopants and the $W_{18}O_{49}$ structure. The Bader charge analysis before and after H adsorption (Fig. 4F) shows a notable shift in charge distribution, indicating that increasing the Ru content modifies the electronic structure of the active sites, making them more favorable for H adsorption. As a result, this electronic structure modulation leads to near-zero adsorption energy on Ru–$W_{18}O_{49}$-5%, which facilitates the HER process.

In summary, we have successfully synthesized urchin-like Ru–$W_{18}O_{49}$ nanospheres assembled from nanorods using a facile hydrothermal method. The resulting catalyst, with a low Ru content of 3.2 wt%, exhibits significantly enhanced acidic HER activity compared to the pristine $W_{18}O_{49}$ nanorods. The exceptional performance can be ascribed to several factors. The Ru doping induces a favorable modulation of the electronic structure, optimizing hydrogen adsorption and increasing the electrochemical surface area. Additionally, the unique urchin-like hierarchical nanostructure, composed of vertically aligned nanorods, offers several advantages: effective contact with the electrolyte, a large surface area, rapid electron transfer, and efficient bubble detachment, all of which collectively contribute to the enhanced HER rate.

This work was supported by the National Natural Science Foundation of China (21771018 and 21875004), the Beijing Natural Science Foundation and Xiaomi Joint Grants (L223011), and the Beijing University of Chemical Technology (buctrc201901).

Data availability

The data supporting this article have been included as part of the ESI.†

Conflicts of interest

There are no conflicts to declare.

References

1 H. Wu, C. Feng, L. Zhang, J. Zhang and D. P. Wilkinson, *Electrochem. Energy Rev.*, 2021, **4**, 473–507.

2 Y. Du, J. Liu, J. Chen, S. Wang, Y. Tang, A. L. Wang, G. Fu and X. F. Lu, *Adv. Energy Mater.*, 2025, **15**, 2404113.

3 J. N. Hansen, H. Prats, K. K. Toudahl, N. Mørch Secher, K. Chan, J. Kibsgaard and I. Chorkendorff, *ACS Energy Lett.*, 2021, **6**, 1175–1180.

4 U. Arshad, J. Tang and Z. Shao, *SusMat*, 2025, **5**, e267.

5 C. Cai, H. Lee, W. Shi, Y. Liu, B. Zhang, L. Sun and T. Wang, *ACS Energy Lett.*, 2025, **10**, 1483–1490.

6 B. Liu, Y. Cheng, B. Cao, M. Hu, P. Jing, R. Gao, Y. Du, J. Zhang and J. Liu, *Appl. Catal., B*, 2021, **298**, 120630.

7 T. Yan, S. Chen, W. Sun, Y. Liu, L. Pan, C. Shi, X. Zhang, Z.-F. Huang and J.-J. Zou, *ACS Appl. Mater. Interfaces*, 2023, **15**, 6912–6922.

8 S. Yu, X. Yu, H. Yang, F. Li, S. Li, Y. S. Kang and J. Y. Zheng, *J. Energy Chem.*, 2024, **99**, 23–49.

9 Y. Zhang, C. Hang, H. Jiang, X. Zhao, X. Deng, L. Wang, F. Ma and Z. Xu, *Sens. Actuators, B*, 2025, **423**, 136843.

10 J. Yang, P. Jia, Y. Cao and P. Yu, *Int. J. Hydrogen Energy*, 2024, **92**, 333–341.

11 M. U. Amin, H. Zhai, Y. Yuan, L. Ren and C. Zhu, *Mater. Today Commun.*, 2024, **39**, 108829.

12 F. Salleh, M. N. A. Tahari, A. Samsuri, T. S. T. Saharuddin, S. S. Sulhadi and M. A. Yarmo, *Int. J. Hydrogen Energy*, 2021, **46**, 24814–24830.

13 C. Peng, W. Zhao, Z. Kuang, J. T. Miller and H. Chen, *Appl. Catal., A*, 2021, **623**, 118293.

14 R. Wu, S.-Q. Guo, Y.-C. Li, M.-Y. Qi, B.-H. Ge and J.-M. Song, *Sens. Actuators, B*, 2024, **410**, 135671.

15 J. Zheng, R. Xia, N. Yaqoob, P. Kaghazchi, J. E. Ten Elshof and M. Huijben, *ACS Appl. Mater. Interfaces*, 2024, **16**, 8616–8626.

16 X. Sun, W. Wu, N. Liu, P. Li, X. Zhao, Z. Qu, K. Zhao, B. Wang, X. Rong and X. Zhang, *Chem. Eng. J.*, 2024, **499**, 156109.

17 Q. Ruan, J. Liu, D. Li, X. Zhang, L. Liu, C. Huang, B. Wang and P. K. Chu, *ACS Appl. Mater. Interfaces*, 2024, **16**, 39266–39276.

18 H. Guo, L. Pan, M. Gao, L. Kong, J. Zhang, A. Khan, N. A. Siddiqui and J. Lin, *Chem. – Eur. J.*, 2024, **30**, e202403043.

19 X. Feng, T. Sun, X. Feng, L. Chen, Y. Yang and F. Zhang, *ACS Appl. Mater. Interfaces*, 2022, **14**, 54769–54780.

20 L. Quan, H. Jiang, G. Mei, Y. Sun and B. You, *Chem. Rev.*, 2024, **124**, 3694–3812.

21 J. K. Nørskov, T. Bligaard, A. Logadottir, J. Kitchin, J. G. Chen, S. Pandelov and U. Stimming, *J. Electrochem. Soc.*, 2005, **152**, J23.